

Chiral Sculptured Thin Films for Circular Polarization of Mid-Wavelength Infrared Light

Vikas Vepachedu and Akhlesh Lakhtakia

Department of Engineering Science and Mechanics, The Pennsylvania State University,
University Park, PA 16802, USA
akhlesh@psu.edu

Abstract

Being an assembly of identical upright helixes, a chiral sculptured thin film (CSTF) exhibits the circular Bragg phenomenon and can therefore be used as a circular-polarization filter in a spectral regime called the circular Bragg regime. This has been already demonstrated in the near-infrared and short-wavelength infrared regimes. If two CSTFs are fabricated in identical conditions to differ only in the helical pitch, and if both are made of a material whose bulk refractive index is constant in a wide enough spectral regime, then the center wavelengths of the circular Bragg regimes of the two CSTFs must be in the same ratio as their helical pitches by virtue of the scale invariance of the frequency-domain Maxwell postulates. This theoretical result was confirmed by measuring the linear-transmittance spectrums of two zinc-selenide CSTFs with helical pitches in the ratio 1:7.97. The center wavelengths were found to be in the ratio 1:7.1, the deviation from the ratio of helical pitches being explainable at least in part because the bulk refractive index of zinc selenide decreased a little with wavelength. We concluded that CSTFs can be fabricated to function as circular-polarization filters in the mid-wavelength infrared regime.

1 Introduction

The production of circularly polarized light from either an unpolarized or a partially polarized source involves the removal of either the left-circularly polarized or the right-circularly polarized component. One way of accomplishing this removal is by inserting a rotated linear polarizer between two orthogonally oriented quarter-wave plates. Relying on the anisotropy of the material that it is made of, a quarter-wave plate [1, pp. 20-21] converts linearly polarized light into circularly polarized light and vice versa. A Fresnel rhomb [1, p. 49] also converts linearly polarized light into circularly polarized light, but without reliance on anisotropy. Instead, its operation is based on the difference between the phase shifts of totally internally reflected light of two orthogonal linear polarization states.

Another way is to use a slab of a structurally chiral medium (SCM), exemplified by cholesteric liquid crystals (CLCs) [2, 3] and chiral sculptured thin films (CSTFs) [4]. As an SCM is helicoidally nonhomogeneous along a fixed axis, it displays the circular Bragg phenomenon in a specific spectral regime called the circular Bragg regime. This phenomenon is the almost total reflection of the incident light of one circular polarization state but very little reflection of the incident light of the other circular polarization state, provided that the thickness L of the SCM is sufficiently high [5]. Depending on the structural period P as well as the relative permittivity dyadic $\underline{\underline{\epsilon}}_{\text{rel}}$ of the SCM, the spatiotemporal manifestation of

the circular Bragg phenomenon is the formation of a light pipe that bleeds energy backward inside the SCM under appropriate conditions [6, 7].

The center wavelength λ_0^{Br} of the circular Bragg regime depends on P . Typically, $\lambda_0^{\text{Br}}/P > 1$ for normal incidence because all eigenvalues of the relative permittivity dyadics of CLCs and CSTFs exceed unity, and the ratio L/P has to be in the neighborhood of 10 or higher for adequately strong manifestation of the circular Bragg phenomenon [5, 8].

Both CLCs [9, 10, 11, 12] and CSTFs [13, 14, 15, 16] have been demonstrated to serve as circular-polarization filters in the visible and the near-infrared (NIR) regimes, because CLCs with $P \lesssim 700$ nm [17, 18, 19] and CSTFs with $P \leq 800$ nm [14, 15, 20] are commonplace. CLCs with periods as large as about 6000 nm have been reported [21], to our knowledge. But the fabrication of stable CLCs with the ratio L/P in the neighborhood of 10 becomes challenging as P increases [22, 23]. One reason is that surface alignment forces invoked by the use of a textured substrate become less efficacious as the ratio L/P increases [22]. Another reason is the enhancement of internal stresses which are inimical to the needed structural chirality of the ordered layering of aciculate molecules becomes poor [23]. CLCs are also sensitive to changes in temperature and pressure [2, 3]. Therefore, although CLCs are suitable for use as circular-polarization filters also in the short-wavelength infrared (SWIR) regime (wavelength $\lambda_0 \in (1400, 3000)$ nm) [24], similar use in the mid-wavelength infrared (MWIR) regime ($\lambda_0 \in (3000, 8000)$ nm) appears not to be easily possible.

CSTFs are solid-state analogs of chiral liquid crystals. Ideally, a CSTF is an assembly of parallel helices of pitch P and rise angle χ . Structural chirality is thus rigidly built in the CSTF morphology, so that neither surface alignment forces have to be invoked nor are internal stresses deleterious. The CSTF morphology is immune to small changes of pressure and temperature, but protection against moisture intake may be necessary [25].

Therefore, with the aim of developing MWIR circular-polarization filters, we decided to fabricate CSTFs with P as high as 5880 nm. Zinc selenide (ZnSe) was chosen because its bulk refractive index varies quite slowly with λ_0 in the MWIR regime [26] and because it is easy to deposit CSTFs [20, 28] of this material by oblique-angle thermal evaporation [29, 30]. The ratio L/P was kept as large as practicable with our thermal evaporation system that was designed for CSTFs to function in the visible regime and is definitely suboptimal for industrial use to fabricate very thick CSTFs needed for the longer wavelengths in the MWIR regime. We also measured the normal-incidence transmittance characteristics of the fabricated CSTFs.

The plan of this paper is as follows. A brief description of theory underlying the transmission of light is presented in Sec. 2.2.1 followed by a discussion in Sec. 2.2.2 of the premise of this research. Fabrication of five different CSTFs is described in Sec. 3.3.1 and experimental methods for their morphological and optical characterization are presented in Secs. 3.3.2 and 3.3.3, respectively. Scanning-electron micrographs of all CSTFs fabricated for this research are presented in Sec. 4.4.1. Theoretical spectrums of the transmittances of a reference CSTF are provided in Sec. 4.4.2 to understand the very limited experimental spectrums of the fabricated CSTFs in Sec. 4.4.3. The paper ends with some remarks in Sec. 5.

2 Theoretical Preliminaries

2.1 Optical Transmission

Suppose the region $0 \leq z \leq L$ is occupied by a CSTF, while the half spaces $z \leq 0$ and $z \geq L$ are vacuum. The linear dielectric properties of the CSTF are delineated by the unidirectionally nonhomogeneous relative permittivity dyadic [30]

$$\begin{aligned} \underline{\underline{\varepsilon}}_r(z, \lambda_0) = \underline{\underline{S}}_z(h, z, P) \cdot \underline{\underline{S}}_y(\chi) \cdot \left[\varepsilon_a(\lambda_0) \mathbf{u}_z \mathbf{u}_z + \varepsilon_b(\lambda_0) \mathbf{u}_x \mathbf{u}_x \right. \\ \left. + \varepsilon_c(\lambda_0) \mathbf{u}_y \mathbf{u}_y \right] \cdot \underline{\underline{S}}_y^{-1}(\chi) \cdot \underline{\underline{S}}_z^{-1}(h, z, P), \quad 0 \leq z \leq L. \end{aligned} \quad (1)$$

Here and hereafter, an $\exp(-i\omega t)$ dependence on time t is implicit with $\omega = 2\pi c_0/\lambda_0$ as the angular frequency and $i = \sqrt{-1}$; c_0 is the speed of light in free space; and \mathbf{u}_x , \mathbf{u}_y , and \mathbf{u}_z are the unit vectors in a Cartesian coordinate system.

The helicoidal nonhomogeneity of the CSTF is captured by the rotation dyadic

$$\begin{aligned} \underline{\underline{S}}_z(h, z, P) = \mathbf{u}_z \mathbf{u}_z + (\mathbf{u}_x \mathbf{u}_x + \mathbf{u}_y \mathbf{u}_y) \cos\left(\frac{2\pi z}{P}\right) \\ + h (\mathbf{u}_y \mathbf{u}_x - \mathbf{u}_x \mathbf{u}_y) \sin\left(\frac{2\pi z}{P}\right). \end{aligned} \quad (2)$$

The direction of the nonhomogeneity is parallel to the z axis. The CSTF is structurally right-handed when $h = 1$, but is structurally left-handed when $h = -1$. The dyadic

$$\underline{\underline{S}}_y(\chi) = \mathbf{u}_y \mathbf{u}_y + (\mathbf{u}_x \mathbf{u}_x + \mathbf{u}_z \mathbf{u}_z) \cos \chi + (\mathbf{u}_z \mathbf{u}_x - \mathbf{u}_x \mathbf{u}_z) \sin \chi \quad (3)$$

represents the *locally* aciculate morphology of the CSTF, with $\chi > 0$ deg being the rise angle.

A 4×4 -matrix-based procedure to calculate the linear and circular remittances of the CSTF of thickness L for normally incident monochromatic light is explained elsewhere [30, Chap. 9] in detail. Using this procedure, we calculated the four linear transmittances ($T_{ss,sp,ps,pp}$) and the four circular transmittances ($T_{RR,RL,LR,LL}$) as functions of λ_0 . Here, T_{sp} is the fraction of the incident power transmitted via an s -polarized plane wave when the incident plane wave is p polarized, T_{LR} is the fraction of the incident power transmitted via a *Left*-circularly polarized plane wave when the incident plane wave is *Right*-circularly polarized, and so on.

2.2 Research Premise

The premise of our research effort can now be explained using the sourceless versions of the frequency-domain Maxwell postulates:

$$\left. \begin{aligned} \nabla \cdot \mathbf{E}(\mathbf{r}, \lambda_0) &= 0 \\ \nabla \cdot \mathbf{H}(\mathbf{r}, \lambda_0) &= 0 \\ \nabla \times \mathbf{E}(\mathbf{r}, \lambda_0) &= i \frac{2\pi c_0}{\lambda_0} \mu_0 \mathbf{H}(\mathbf{r}, \lambda_0) \\ \nabla \times \mathbf{H}(\mathbf{r}, \lambda_0) &= -i \frac{2\pi c_0}{\lambda_0} \varepsilon_0 \underline{\underline{\varepsilon}}_r(z, \lambda_0) \cdot \mathbf{E}(\mathbf{r}, \lambda_0) \end{aligned} \right\}. \quad (4)$$

Here, ε_0 is the permittivity and μ_0 is the permeability of free space.

Let us scale all space isotropically as

$$\mathbf{r}' = \alpha \mathbf{r}, \quad (5)$$

where the scaling parameter $\alpha > 1$ is real. If we also scale the free-space wavelength as

$$\lambda'_0 = \alpha \lambda_0, \quad (6)$$

Eqs. (4) can be recast as

$$\left. \begin{aligned} \nabla' \cdot \mathbf{E}(\mathbf{r}', \lambda'_0) &= 0 \\ \nabla' \cdot \mathbf{H}(\mathbf{r}', \lambda'_0) &= 0 \\ \nabla' \times \mathbf{E}(\mathbf{r}', \lambda'_0) &= i \frac{2\pi c_0}{\lambda'_0} \mu_0 \mathbf{H}(\mathbf{r}', \lambda'_0) \\ \nabla' \times \mathbf{H}(\mathbf{r}', \lambda'_0) &= -i \frac{2\pi c_0}{\lambda'_0} \varepsilon_0 \underline{\underline{\varepsilon}}_r(z', \lambda'_0) \cdot \mathbf{E}(\mathbf{r}', \lambda'_0) \end{aligned} \right\}. \quad (7)$$

Provided that

$$\underline{\underline{\varepsilon}}_r(z', \lambda'_0) = \underline{\underline{\varepsilon}}_r(z, \lambda_0), \quad (8)$$

the solutions of Eqs. (4) and (7) shall be identical [31].

In other words, if we can fabricate two CSTFs such that

- (i) their helixes have rise angles χ_1 and $\chi_2 = \chi_1$,
- (ii) their helixes have pitches P_1 and $P_2 = \alpha P_1$, and
- (iii) their thicknesses are L_1 and $L_2 = \alpha L_1$,

then the transmittances of the first CSTF at $\lambda_0 = \lambda_{01}$ shall be the same as the transmittances of the second CSTF at $\lambda_0 = \lambda_{02} = \alpha \lambda_{01} > \lambda_{01}$ if the relative permittivity dyadic $\underline{\underline{\varepsilon}}_r^{(1)}$ of the first CSTF and the relative permittivity dyadic $\underline{\underline{\varepsilon}}_r^{(2)}$ of the first CSTF satisfy the condition

$$\underline{\underline{\varepsilon}}_r^{(2)}(\alpha z, \lambda_{02}) = \underline{\underline{\varepsilon}}_r^{(1)}(z, \lambda_{01}). \quad (9)$$

Therefore, if both CSTFs are made by evaporating a dielectric material whose bulk relative permittivity is uniform in a spectral regime that encompasses both λ_{0_1} and $\alpha\lambda_{0_1}$, and if the first CSTF can serve as a circular-polarization filter in a spectral regime encompassing λ_{0_1} , then the second CSTF must serve as a circular-polarization filter in a spectral regime encompassing $\alpha\lambda_{0_1}$.

ZnSe was chosen for evaporation because its bulk refractive index n_{ZnSe} varies weakly with λ_0 in the MWIR regime [26, 27]. Since n_{ZnSe} generally decreases as λ_0 increases, as shown in Fig. 1, the second CSTF will perform as a circular-polarization filter in a spectral regime encompassing wavelengths somewhat smaller than $\alpha\lambda_{0_1}$.

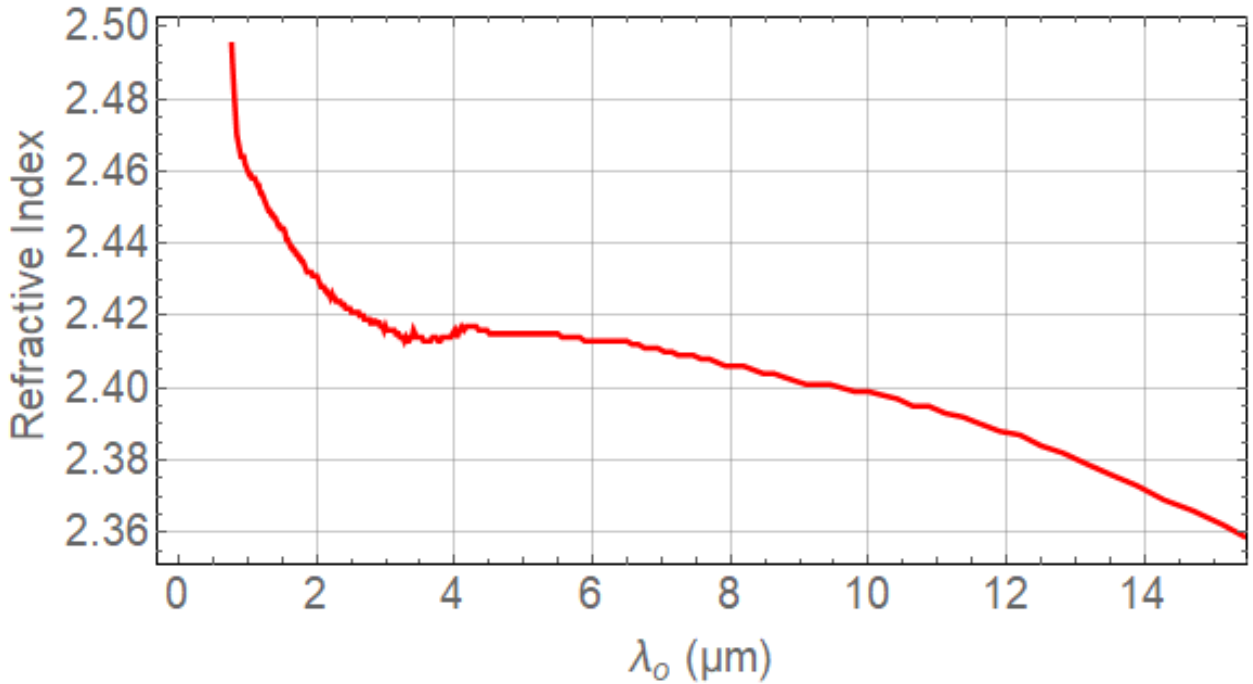


Figure 1: Real part of n_{ZnSe} as a function of λ_0 . The imaginary part of n_{ZnSe} does not exceed 10^{-6} in the same spectral regime [27].

3 Experimental Methods

3.1 Fabrication of CSTFs

Five different structurally right-handed CSTFs were fabricated using oblique-angle thermal evaporation, the targeted values of their structural period P and number of periods L/P being listed in Table 1.

Thermal evaporation system was carried out in a low-pressure chamber (Torr International, New Windsor, New York). Inside this chamber, the material to be evaporated is kept

Table 1: CSTF Samples Fabricated

Sample No.	Targeted P (nm)	Measured P (nm)	L/P	τ (s)	Number of Depositions
1	366	364	10	5.955	3
2	732	727	10	12.627	5
3	1464	1410	10	25.971	10
4	2928	2900	10	52.658	20
5	5856	5880	1	106.033	4

in a tungsten boat (S22-.005W, R. D. Mathis, Long Beach, California) which can be heated by passing a current through it. About 15 cm above the boat is a substrate holder whose rotations about two mutually orthogonal axes are controlled by two stepper motors. One axis of rotation passes normally through the substrate holder to serve as the z axis, and the second serves as the y axis in the substrate (xy) plane. There is also a quartz crystal monitor (QCM) in the chamber which has been calibrated to measure the thickness of the film as it is being deposited. Finally, a shutter between the boat and the substrate holder allows the user to abruptly start or halt the deposition as needed.

99.995 % pure ZnSe (Alfa Aesar, Ward Hill, Massachusetts) was the material of choice for the reasons discussed previously. The manufacturer supplied ZnSe lumps that were crushed into a fine powder. When crushing the lumps, a respirator mask, gloves, and a lab coat were worn to avoid the toxic effects of ZnSe exposure [32].

Each CSTF was deposited on two substrates simultaneously, one being either glass or silicon and the other being silicon. The sample grown on the first substrate was optically characterized. If the value of P was chosen for the circular Bragg regime to lie in the visible regime or the NIR regime or the SWIR regime, a pre-cleaned glass slide (48300-0025, VWR, Radnor, Pennsylvania) was used as the first substrate. If the value of P was chosen for the circular Bragg regime to lie in the MWIR regime, silicon was used as the first substrate. The morphology of the sample grown on the second substrate was characterized on a scanning-electron microscope.

Each substrate was cleaned in an ethanol bath using an ultrasonicator for 9 min on each side; thereafter, the substrate was immediately dried with pressurized nitrogen gas. Both substrates were secured to the substrate holder using Kapton tape (S-14532, Uline, Pleasant Prairie, Wisconsin), being positioned as close to the center of the holder as possible to ensure that they would be directly above the tungsten boat. The shutter was rotated to prevent any vapor from reaching the two substrates.

To begin the deposition process, the low-pressure chamber was pumped down to approximately 1 μ Torr. Next, the current was gradually increased to ~ 100 A and the shutter was

rotated to allow a collimated portion of the ZnSe vapor to reach the substrates. The deposition rate was manually maintained at $0.4 \pm 0.02 \text{ nm s}^{-1}$, using the QCM. Upon completion of the deposition, the shutter was rotated to prevent the vapor from reaching the substrates and the current was quickly brought down to 0 A to prevent any further deposition. After the deposition, the chamber was allowed to cool for at least 30 min before it was opened.

Given the desired thickness of the CSTF, the deposition rate, and the limited amount of ZnSe that could be put in the boat, multiple depositions were needed to fabricate the CSTF. The number of depositions for each of the five samples is shown in Table 1. During each deposition, a film of maximum thickness 1500 nm could be deposited before the ZnSe powder loaded in the boat was depleted. Between these depositions, the boat was refilled with ZnSe powder and, if needed, the quartz crystal in the QCM was replaced.

During every deposition, the angle of the collimated vapor flux with respect to the substrate plane was set at $\chi_v = 20 \text{ deg}$. Furthermore, the substrate was rotated about the z axis in accordance with the M:1 asymmetric serial bi-deposition technique [28, 33] as follows. A subdeposit was made for time τ , followed by a rapid rotation about the z axis by 180 deg in 0.406 s, followed by another subdeposit for time τ/M , followed by a rapid rotation about the z axis by 183 deg in 0.413 s. This 4-step process was iterated 120 times in order to deposit a single period. Based on a detailed comparative study to improve the exhibition of the circular Bragg phenomenon [28], we fixed $M = 7$ for all CSTFs. The value of τ chosen for each CSTF fabricated is listed in Table 1.

3.2 Morphological Characterization

The cross-sectional morphologies of all five CSTFs fabricated on a silicon substrate were characterized using the FEI NovaTM NanoSEM 630 (FEI, Hillsboro, Oregon) field-emission scanning-electron microscope. Prior to taking the images, the sample was cleaved using the freeze-fracture technique [34] so that cross-sectional images could be taken on a clean cleaved edge free from edge-growth effects. The sample was then sputtered with iridium using a Quorum Emitech K575X (Quorum Technologies, Ashford, Kent, United Kingdom) sputter coater before imaging.

3.3 Optical Characterization

Optical characterization of two of the five CSTFs fabricated was performed within 24 h of fabrication, the sample being contained in a desiccator before characterization to prevent degradation due to moisture adsorption. A custom-built apparatus was used to measure the linear and circular transmittances of sample 1 [28, 35], and a Vertex 70 spectrophotometer (Bruker, Billerica, Massachusetts) was used to measure the linear transmittances of sample 4.

The transmittance-measurement apparatus for $\lambda_0 \in [600 \text{ nm}, 900 \text{ nm}]$ is described in detail elsewhere [28, 35]. Briefly, light from a halogen source (HL-2000, Ocean Optics, Dunedin, Florida) was passed through a fiber-optic cable and then through a linear polarizer (GT10, ThorLabs, Newton, New Jersey); it was transmitted through the sample to be characterized

and then passed through a second linear polarizer (GT10, ThorLabs) and a fiber-optic cable to a CCD spectrometer (HRS-BD1-025, Mightex Systems, Pleasanton, California) [35]. The linear transmittances were thus measured for normal incidence. For measurements of the circular transmittances, a Fresnel rhomb (LMR1, ThorLabs) was introduced directly after the first linear polarizer and another Fresnel rhomb directly before the second linear polarizer [28]. All measurements were taken in a dark room to avoid noise from external sources.

The experimental setup for the Vertex 70 spectrophotometer was different. As only one linear polarizer was available, it was used on the incidence side so that only the sums $T_s = T_{ss} + T_{ps}$ and $T_p = T_{pp} + T_{sp}$ were measured for normal incidence.

4 Results and Discussion

4.1 Morphology

Figure 2 presents cross-sectional scanning-electron micrographs of all five samples listed in Table 1. Table 1 presents the value of P of every sample fabricated, as estimated from its micrograph. The discrepancy between the targeted and measured values of P is less than 1% for four of the five samples, and just 3.7% for sample 3. The discrepancy is due to the variability inherent in manual control of the deposition rate. We expect that even better agreement will be obtained after the fabrication process has been optimized for industrial production.

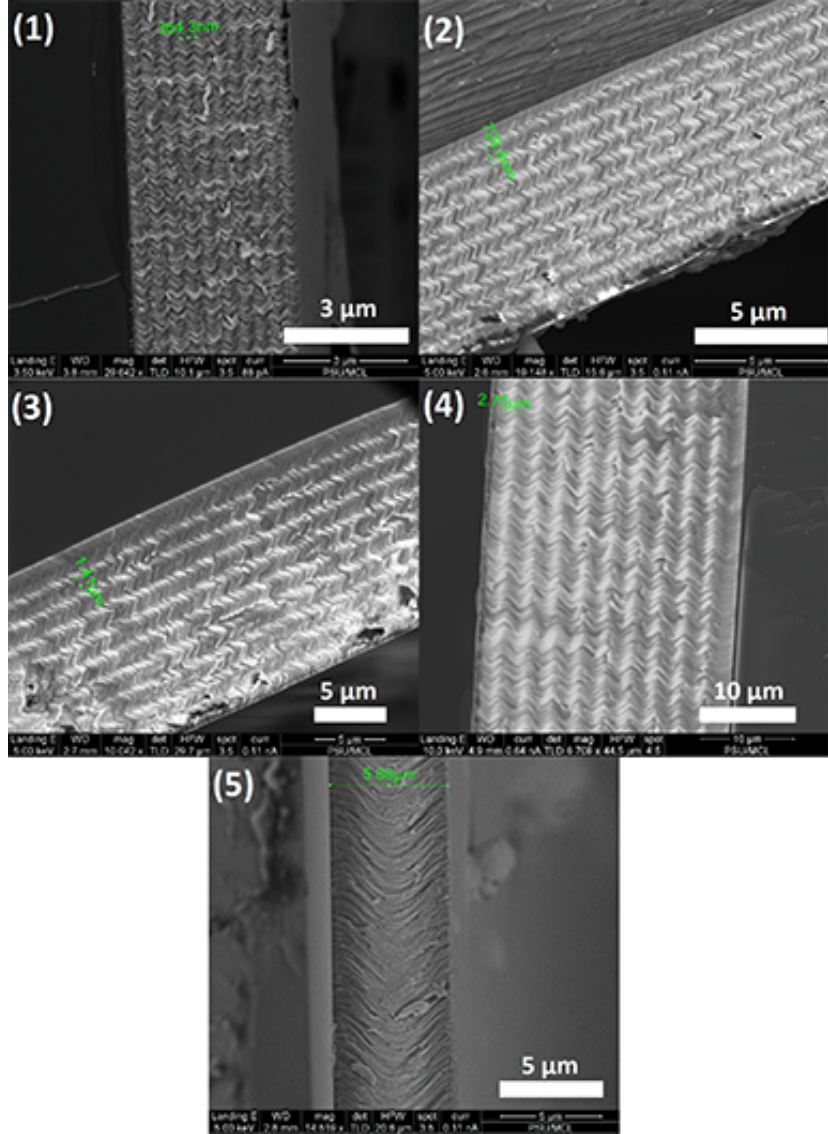


Figure 2: Cross-sectional scanning-electron micrographs of all five CSTF samples listed in Table 1.

Each of the five micrographs clearly shows that the fabricated CSTF is an array of very similar helices. Even sample 5—which has just one period because the long duration required to fabricate many periods of that CSTF is infeasible with the resources of an academic laboratory—is an array of helices. The morphologies of all five samples being the same, except for the scale factor α in Eq. (6), we conclude that it is possible to fabricate CSTFs with periods on the order of several micrometers to serve as circular-polarization filters in the MWIR regime.

4.2 Reference Theoretical Results

In order to provide theoretical results to serve as a reference for our experimental findings, we assumed that the eigenvalues ε_a , ε_b and ε_c of $\underline{\underline{\varepsilon}}_r$ to have single-resonance Lorentzian dependences [36] on λ_0 . Thus,

$$\varepsilon_\ell(\lambda_0) = 1 + \frac{p_\ell}{1 + (1/N_\ell - i\lambda_\ell/\lambda_0)^2}, \quad \ell \in \{a, b, c\}, \quad (10)$$

with the oscillator strengths denoted by p_ℓ . Accordingly, the resonance wavelengths are $\lambda_\ell (1 + N_\ell^{-2})^{-1/2}$ and the linewidths are λ_ℓ/N_ℓ , $\ell \in \{a, b, c\}$. Calculations of all transmittances, linear as well as circular, of a reference CSTF for normal incidence were made by setting [37]: $p_a = 4.7$, $p_b = 5.2$, $p_c = 4.6$, $\lambda_{a,c} = 260$ nm, $\lambda_b = 270$ nm, $N_{a,b,c} = 130$, $\chi = 50$ deg, $h = 1$, $P = 324$ nm, and $L = 20P$.

Figure 3 shows all four circular transmittances of the reference CSTF for normal incidence. As this CSTF is structurally right-handed, the circular Bragg phenomenon is evident as a trough centered at $\lambda_0 \approx 818$ nm in the spectrum of T_{RR} , but that feature is absent in the spectrums of the other three circular transmittances. A comparison of the spectrums of T_{RR} and T_{LL} shows clearly that the reference CSTF can function as a circular-polarization filter at and in the neighborhood of $\lambda_0 = 818$ nm, which is the center wavelength of the circular Bragg regime.

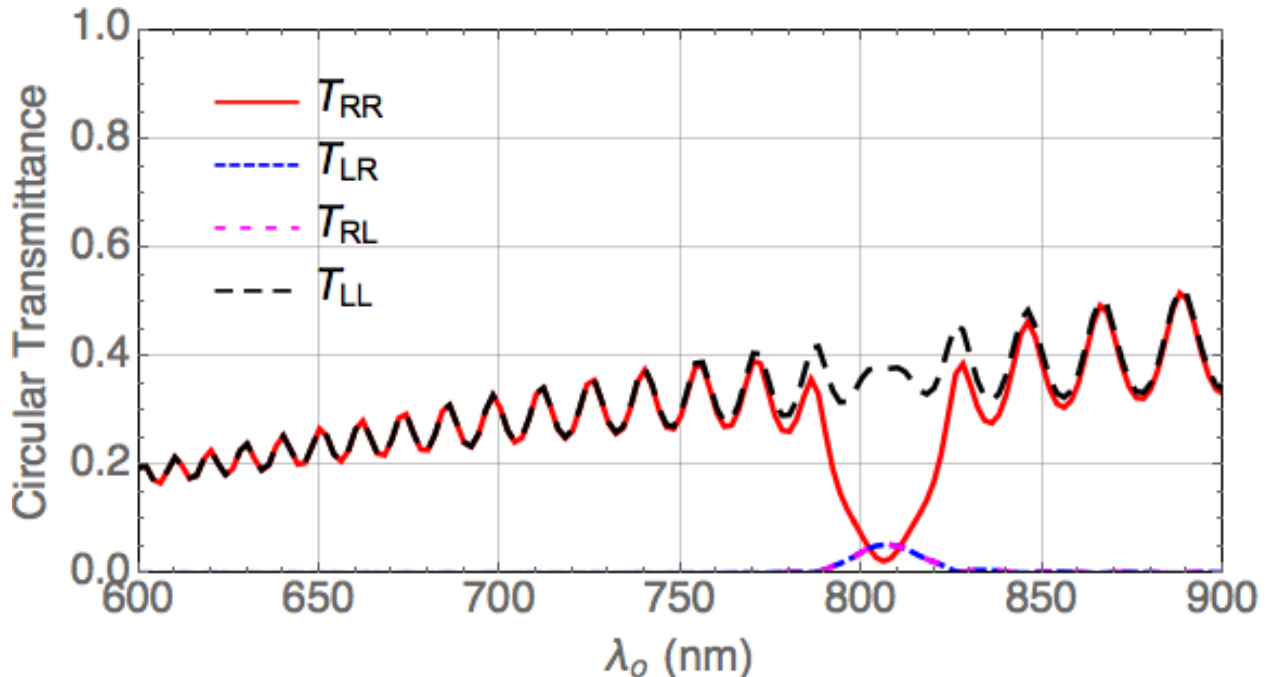


Figure 3: Calculated spectrums of the circular transmittances of the reference CSTF described in Sec. 4.4.2.

The center wavelength is about 2.52 times the period 324 nm used for the calculations. If the period were increased by a factor $\alpha > 1$, then the center wavelength would also

be increased by the same factor provided that the bulk refractive index of the evaporated material remained invariant, as discussed in Sec. 2.2.2. ZnSe *almost* fulfills that requirement, as shown in Fig. 1. Hence, we can conclude that samples 2–4 should function as circular-polarization filters in progressively longer-wavelength regimes than the one in which sample 1 does; furthermore, the same would be true if sample 5 were to be fabricated with a sufficiently large number of periods [5, 8] instead of just one.

As apparatus to measure the circular transmittances at longer wavelengths may not be available, we provide the spectrums of all four linear transmittances of the reference CSTF in Fig. 4. These spectrums could allow us to properly compare the experimental data on linear transmittances of the larger- P samples with theory. In Fig. 4 we notice a distinctive feature in the circular Bragg regime. The troughs of T_{ss} and T_{pp} intersect at $\lambda_0 \approx 818$ nm. If that pattern were to be observed in the experimental results for a given sample in a spectral regime in which the circular Bragg phenomenon is expected, one could infer the existence of that phenomenon even if circular transmittances could not be measured.

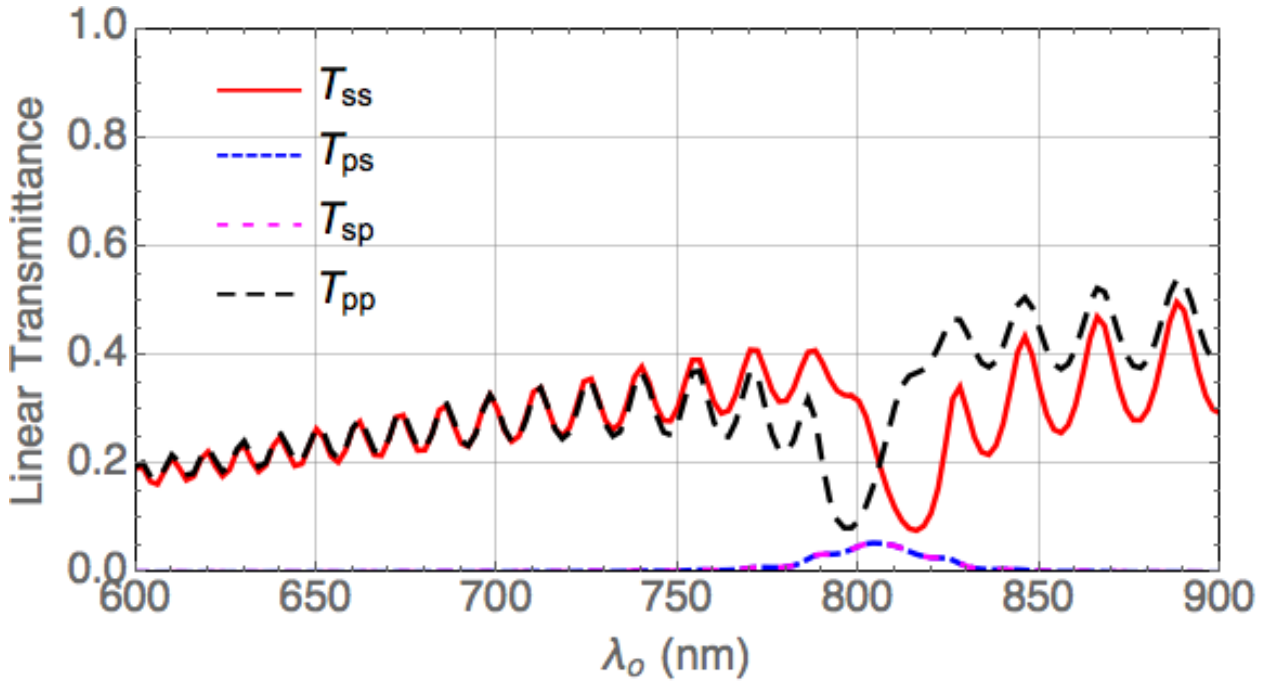


Figure 4: Calculated spectrums of the linear transmittances of the reference CSTF described in Sec. 4.4.2.

4.3 Experimental Results

Figure 5 contains the experimentally determined spectrums of the four circular transmittances of sample 1 ($P = 364$ nm, $L = 10P$). These spectrums qualitatively match those of the reference CSTF in Fig. 3, sample 1 exhibiting a circular Bragg regime centered at $\lambda_0 \approx 780$ nm. At this wavelength, the difference between $T_{LL} = 0.691$ and $T_{RR} = 0.239$

is large enough so that sample 1 can be taken to function as a rejection filter for incident right-circularly polarized light but not for incident left-circularly polarized light. Further improvement may come by increasing the number of periods, i.e., by increasing the ratio L/P , as has been established theoretically [5, 8].

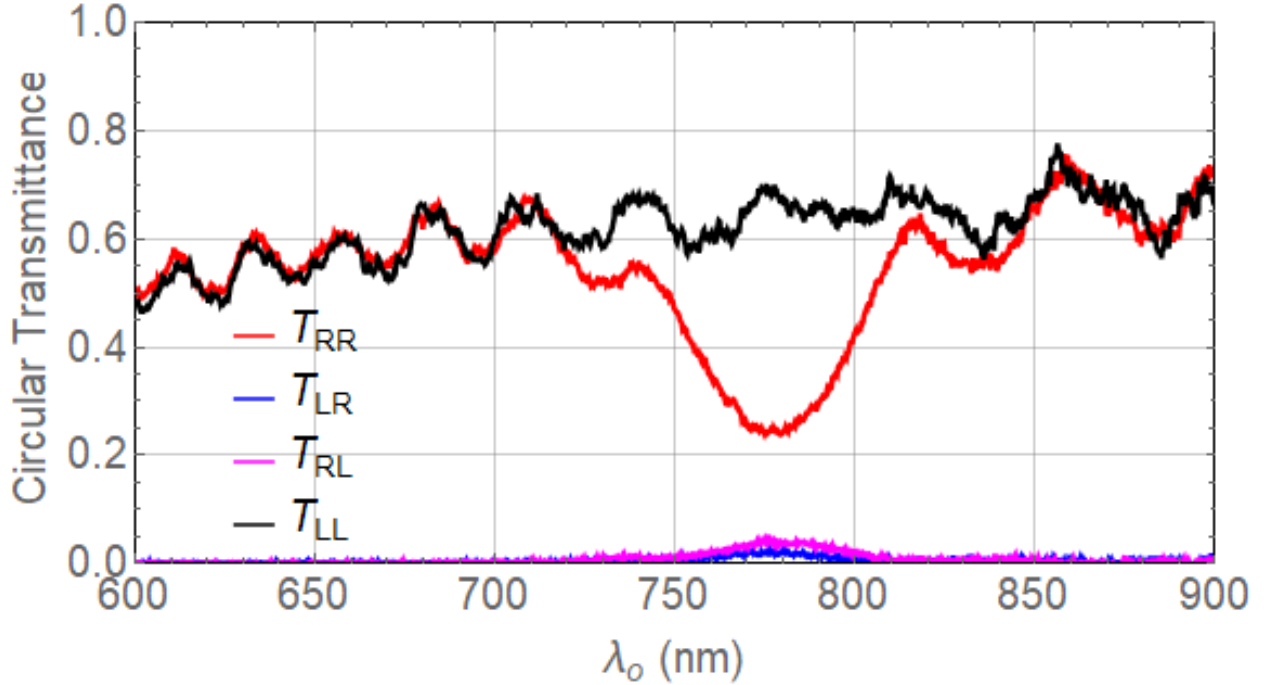


Figure 5: Measured spectrums of the circular transmittances of sample 1.

Figure 6 contains the experimentally determined spectrums of the four linear transmittances of sample 1. These spectrums qualitatively match those of the reference CSTF in Fig. 4, the troughs of T_{ss} and T_{pp} intersect at $\lambda_0 = 761$ nm in Fig. 6. This intersection is very close to 780 nm, the center wavelength of the circular Bragg regime in Fig. 5 for the same CSTF. Thus, by observing the same intersections for samples with larger P , we can verify the exhibition of the circular Bragg phenomenon by those samples.

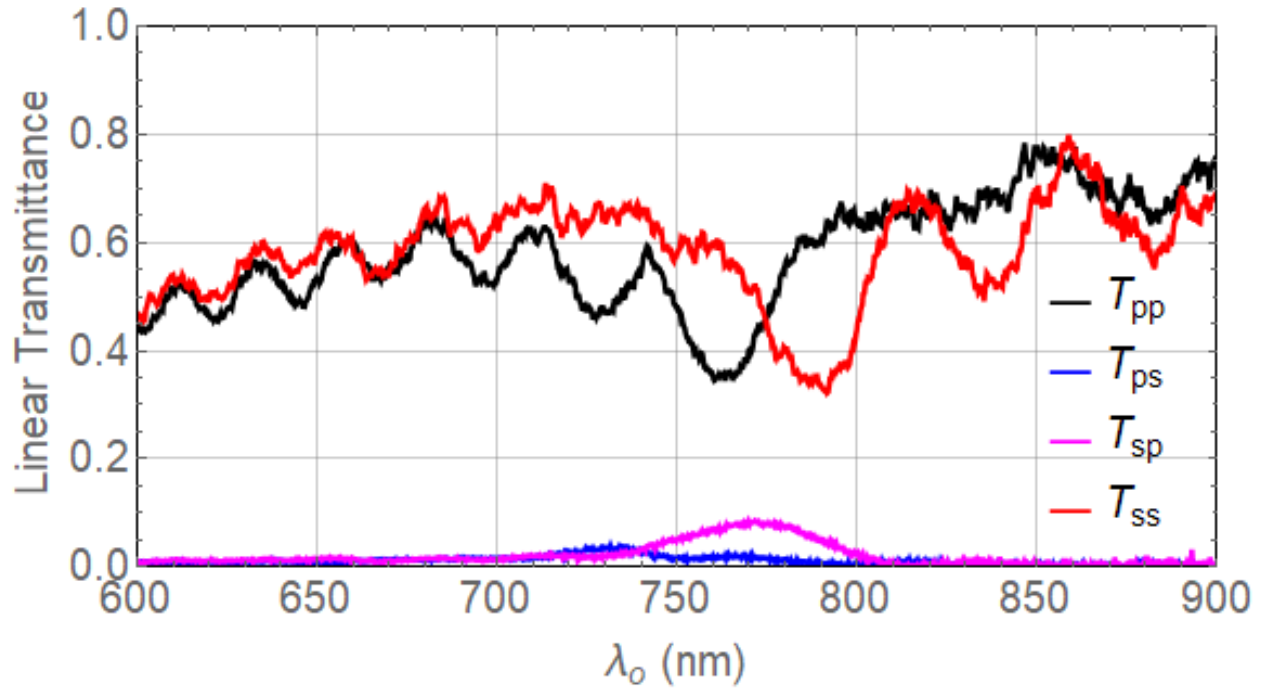


Figure 6: Measured spectrums of the linear transmittances of sample 1.

Accordingly, we can predict that the center wavelength of the circular Bragg regime of sample 4 would be $780\alpha = 6214$ nm, with $\alpha = 2900/364 = 7.97$. The graphs of T_s and T_p in Fig. 7 have peaks that intersect at $\lambda_0 = 5512$ nm, which is lower than 6214 nm. This lowering can be explained by reduction of the bulk relative permittivity of ZnSe by about 3.05% in Fig. 1 as λ_0 increases from 780 nm to 6000 nm.

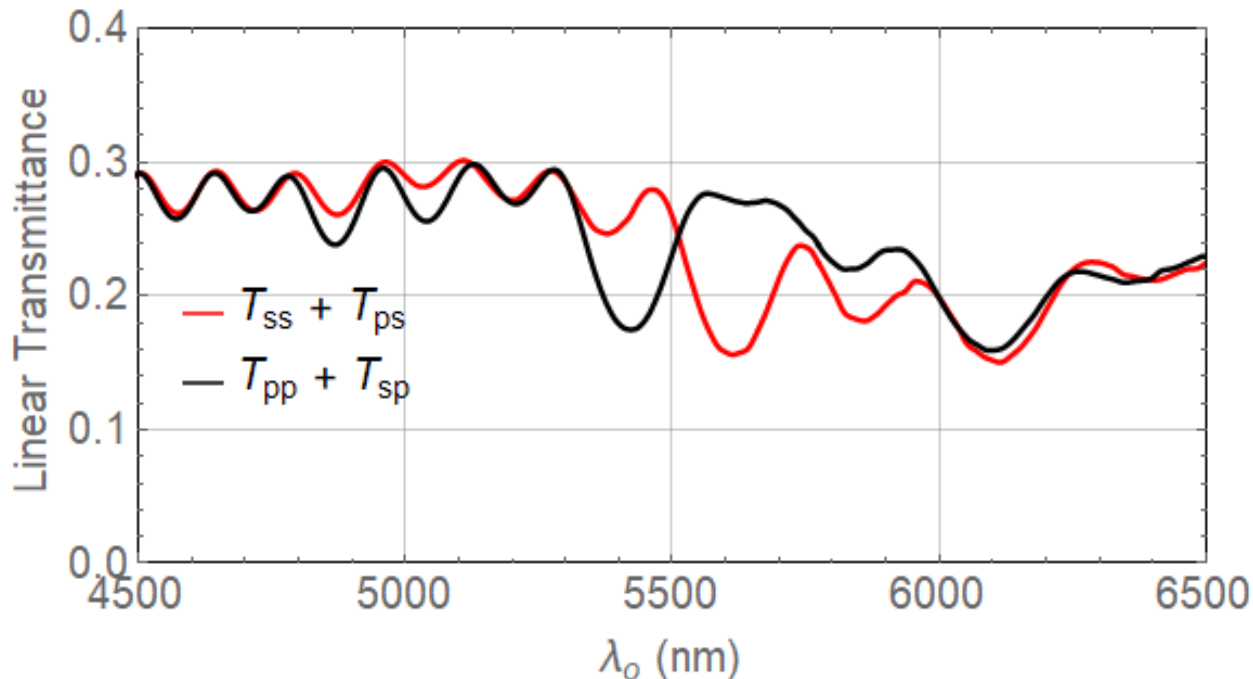


Figure 7: Measured spectrums of $T_s = T_{ss} + T_{ps}$ and $T_p = T_{pp} + T_{sp}$ of sample 4.

Likewise, if a multiple-period version of sample 5 were to be made, then $\alpha = 5880/364 = 16.15$ and the center wavelength of the circular Bragg regime of sample 5 would be somewhat lower than $780\alpha = 12600$ nm. Thus, we have demonstrated that CSTFs can be fabricated to serve as circular-polarization filters in the MWIR regime.

Before closing this section, we must remark that our apparatus were not appropriate to measure diffuse scattering in nonspecular directions. Nevertheless, our conclusion on the performance of CSTFs as circular-polarization filters for normal incidence in the MWIR regime holds.

5 Concluding Remarks

Relying on the scale invariance of the frequency-domain Maxwell postulates [31], we selected a material whose bulk refractive index is very weakly dependent on the wavelength. This material was used as the evaporant material to fabricate five chiral sculptured thin films—of structural periods ranging from ~ 360 nm to ~ 5900 nm—by oblique-angle thermal evaporation. The fabrication conditions of all five CSTFs were thus identical except for a change in scale. Morphological characterization confirmed that each of the five CSTFs was an assembly of parallel helixes, the helical pitches in those CSTFs ranging from ~ 360 nm to ~ 5900 nm.

As expected from the literature [5, 37, 19, 18], the measured circular transmittances of the CSTF of the smallest period demonstrated the circular Bragg phenomenon in the NIR

regime, confirming that CSTFs of sufficient thickness can function as circular-polarization filters in the same regime. The linear transmittances of the CSTF of the smallest period were also measured to identify a spectral feature that would indicate the occurrence of the circular Bragg phenomenon, this spectral feature also being confirmed theoretically. The same feature was experimentally demonstrated to exist in the spectrums of the linear transmittances of a CSTF whose structural period was about 8 times larger than that of the CSTF with the smallest period. Even though the center wavelength of the circular Bragg regime concomitantly increased by a factor of about 7.1, at least in part because the bulk refractive index of the evaporant material decreased a little with λ_0 , we can conclude that CSTFs can be fabricated to function as circular-polarization filters in the MWIR regime.

Acknowledgments. VV thanks Pittsburgh Plate and Glass, Inc., for an undergraduate research fellowship. AL thanks the Charles Godfrey Binder Endowment at Penn State for ongoing support of his research activities.

References

- [1] E. Collett, *Field Guide to Polarization* (SPIE Press, 2005).
- [2] S. Chandrasekhar, *Liquid Crystals*, 2nd ed. (Cambridge University, 1992).
- [3] P. G. de Gennes and J. A. Prost, *The Physics of Liquid Crystals*, 2nd ed. (Clarendon, 1993).
- [4] N. O. Young and J. Kowal, “Optically active fluorite films,” *Nature* **183**, 104–105 (1959).
- [5] M. Faryad and A. Lakhtakia, “The circular Bragg phenomenon,” *Adv. Opt. Photon.* **6**, 225–292 (2014).
- [6] J. B. Geddes III, M. W. Meredith, and A. Lakhtakia, “Circular Bragg phenomenon and pulse bleeding in cholesteric liquid crystals,” *Opt. Commun.* **182**, 45–57 (2000).
- [7] J. B. Geddes III and A. Lakhtakia, “Videopulse bleeding in axially excited chiral sculptured thin films in the Bragg regime,” *Eur. Phys. J. Appl. Phys.* **17**, 21–24 (2002).
- [8] W. D. St. John, W. J. Fritz, Z. J. Lu, and D.-K. Yang, “Bragg reflection from cholesteric liquid crystals,” *Phys. Rev. E* **51**, 1191–1198 (1995).
- [9] J. Adams, W. Haas, and J. Dailey, “Cholesteric films as optical filters,” *J. Appl. Phys.* **42**, 4096–4098 (1971).
- [10] T. J. Scheffer, “Twisted nematic display with cholesteric reflector,” *J. Phys. D: Appl. Phys.* **8**, 1441–1448 (1975).
- [11] S. Ishihara, F. Yokotani, Y. Matsuo, and K. Morimoto, “Preparation and properties of optical notch filters of cholesteric liquid crystals,” *Polymer* **29**, 2141–2145 (1988).

- [12] S. D. Jacobs, K. A. Cerqua, K. L. Marshall, A. Schmid, M. J. Guardalben, and K. J. Skerrett, “Liquid-crystal laser optics: design, fabrication, and performance,” *J. Opt. Soc. Am. B* **5**, 1962–1979 (1988).
- [13] Q. Wu, I. J. Hodgkinson, and A. Lakhtakia, “Circular polarization filters made of chiral sculptured thin films: experimental and simulation results,” *Opt. Eng.* **39**, 1863–1868 (2000).
- [14] Y. J. Park, K. M. A. Sobahan, and C. K. Hwangbo, “Wideband circular polarization reflector fabricated by glancing angle deposition,” *Opt. Express* **16**, 5186–5192 (2008).
- [15] D. P. Pulsifer, R. J. Martín-Palma, S. E. Swiontek, C. G. Pantano, and A. Lakhtakia, “Wideband-rejection filters and reflection-hole filters of chalcogenide glass for circularly polarized IR-A and IR-B radiation,” *Opt. Mater. Express* **1**, 1332–1340 (2011).
- [16] Y. Zhu, F. Zhang, G. You, J. Liu, J. D. Zhang, A. Lakhtakia, and J. Xu, “Stable circularly polarized emission from a vertical-cavity surface-emitting laser with a chiral reflector,” *Appl. Phys. Express* **5**, 032102 (2012).
- [17] K.-H. Kim, H.-J. Jin, K.-H. Park, J.-H. Lee, J. C. Kim, and T.-H. Yoon, “Long-pitch cholesteric liquid crystal cell for switchable achromatic reflection,” *Opt. Express* **18**, 16745–16750 (2010).
- [18] J. Sato, N. Morioka, Y. Teramoto, and Y. Nishio, “Chiroptical properties of cholesteric liquid crystals of chitosan phenylcarbamate in ionic liquids,” *Polymer J.* **46**, 559–567 (2014).
- [19] C. Kulkarni, D. Di Nuzzo, E. W. Meijer, and S. C. J. Meskers, “Pitch and handedness of the cholesteric order in films of a chiral alternating fluorene copolymer,” *J. Phys. Chem. B* **121**, 11520–11527 (2017).
- [20] S. Erten and A. Lakhtakia, “Dual-band circular-polarization filter for obliquely incident light,” *Microw. Opt. Technol. Lett.* **58**, 2381–2384 (2016).
- [21] S.-S. Li, Y. Shen, Z.-N. Chang, W.-S. Li, Y.-C. Xu, X.-Y. Fan, and L.-J. Chen, “Dynamic cholesteric liquid crystal superstructures photoaligned by one-step polarization holography,” *Appl. Phys. Lett.* **111**, 231109 (2017).
- [22] A. Denisov and J.-L. de Bougrenet de la Tocnaye, “Resonant gratings in planar Grandjean cholesteric composite liquid crystals,” *Appl. Opt.* **46**, 6680–6687 (2007).
- [23] N. Kiyoto, *Infrared Light Reflective Film*, US Patent 2012/0026580 A1 (02 Feb 2012).
- [24] W. Zhang, S. Kragt, A. P. H. J. Schenning, L. T. de Haan, and G. Zhou, “Easily processable temperature-responsive infrared-reflective polymer coatings,” *ACS Omega* **2**, 3475–3482 (2017).

- [25] I. J. Hodgkinson, Q. h. Wu, and K. M. McGrath, “Moisture adsorption effects in biaxial and chiral optical thin film coatings,” *Proc. SPIE* **3790**, 184–194 (1999).
- [26] D. T. F. Marple, “Refractive index of ZnSe, ZnTe, and CdTe,” *J. Appl. Phys.* **35**, 539–542 (1964).
- [27] M. Querry, *Optical Constants of Minerals and Other Materials From the Millimeter to the Ultraviolet*. CERDEC U.S. Army RDECOM, Aberdeen, MD, USA (1987).
- [28] P. D. McAtee and A. Lakhtakia, “Reflection and transmission of obliquely incident light by chiral sculptured thin films fabricated using asymmetric serial-bideposition technique,” *J. Nanophoton.* **11**, 043502 (2017).
- [29] D. M. Mattox, *The Foundations of Vacuum Coating Technology* (Noyes Publications, 2003).
- [30] A. Lakhtakia and R. Messier, *Sculptured Thin Films: Nanoengineered Morphology and Optics* (SPIE Press, 2005).
- [31] G. Sinclair, “Theory of models of electromagnetic systems,” *Proc. IRE* **36**, 1364–1370 (1948).
- [32] *Safety Data Sheet*. <https://www.crystran.co.uk/userfiles/files/zinc-selenide-znse-msds.pdf> Crystran, 15 February 2018.
- [33] S. M. Pursel and M. W. Horn, “Prospects for nanowire sculptured thin-film devices,” *J. Vac. Sci. Technol. B* **25**, 2611–2615 (2007).
- [34] N. J. Severs, “Freeze-fracture electron microscopy,” *Nat. Protocols* **2**, 547–576 (2007).
- [35] V. Vepachedu, P. D. McAtee, and A. Lakhtakia, “Nonexhibition of Bragg phenomenon by chevronic sculptured thin films: experiment and theory,” *J. Nanophoton.* **11**, 036018 (2017).
- [36] C. Kittel, *Introduction to Solid State Physics* (Wiley Eastern, 1974).
- [37] S. Erten, A. Lakhtakia, and G. D. Barber, “Experimental investigation of circular Bragg phenomenon for oblique incidence,” *J. Opt. Soc. Am. A* **32**, 764–770 (2015).